

# Crystallite fusion in nanocellulose aggregates

Kazuho Daicho (✉ [daichok@g.ecc.u-tokyo.ac.jp](mailto:daichok@g.ecc.u-tokyo.ac.jp))

The University of Tokyo <https://orcid.org/0000-0003-4203-2257>

Kayoko Kobayashi

Kyoto University

Shuji Fujisawa

The University of Tokyo

Tsuguyuki Saito

The University of Tokyo

---

Physical Sciences - Article

**Keywords:** crystallite, fusion, biopolymers, nanocellulose aggregates

**Posted Date:** May 18th, 2021

**DOI:** <https://doi.org/10.21203/rs.3.rs-518217/v1>

**License:**  This work is licensed under a Creative Commons Attribution 4.0 International License.

[Read Full License](#)

---

# **Crystallite fusion in nanocellulose aggregates**

Kazuho Daicho<sup>1\*</sup>, Kayoko Kobayashi<sup>2</sup>, Shuji Fujisawa<sup>1</sup>, and Tsuguyuki Saito<sup>1\*</sup>

<sup>1</sup>Department of Biomaterial Sciences, Graduate School of Agricultural and Life Sciences, The University of Tokyo, 1-1-1 Yayoi, Bunkyo-ku, Tokyo 113-8657, Japan

<sup>2</sup>Division of Forest and Biomaterials Science, Graduate School of Agriculture, Kyoto University, Sakyo-ku, Kyoto 606-8502, Japan

\*Corresponding author. E-mail: daichok@g.ecc.u-tokyo.ac.jp, saitot@g.ecc.u-tokyo.ac.jp

## Summary

Crystallite refers to a single crystalline grain in crystal aggregates, and multiple crystallites form a grain boundary or the inter-crystallite interface<sup>1</sup>. A grain boundary is a structural defect that hinders the efficient directional transfer of mechanical stress or thermal phonons in crystal aggregates. We observed that grain boundaries within an aggregate of a-few-nanometers-wide fibrillar crystallites of cellulose were crystallized by enhancing their inter-crystallite interactions; multiple crystallites were coupled into single fusion crystals without passing through a melting or dissolving state.

Accordingly, the crystallinity of naturally occurring cellulose, which has previously been considered irreversible once decreased<sup>2</sup>, was recovered, and the thermal energy transfer in the aggregate was significantly improved. Other fibrillar crystallites of chitin also showed a similar fusion phenomenon by enhancing the inter-crystallite interactions. Crystallite fusion in aggregates may occur for other biopolymers.

## Introduction

Mechanical and thermal energy transfers in crystal aggregates are governed by a grain boundary or the interface where multiple crystallites meet<sup>1</sup>. Proper crystallite interactions at the grain boundary can allow mechanical stress or thermal phonons to directionally transfer in the aggregate; however, a grain boundary is a structural defect that deforms under stress or scatters phonons<sup>3,4</sup>. This feature becomes pronounced when the crystallites have nanoscale dimensions and form a large area of the grain boundary. In the field of nanotechnology, it is currently a challenge to exploit the potential of such nanoscale crystallites, including biopolymer fibrils and clay platelets, in bulk aggregates or composites by tailoring the interactions between crystallites or with other components<sup>5-7</sup>.

Ideal energy transfer in crystal aggregates must be realised by crystallization of the grain boundary. If multiple crystallites can be coupled into single fusion crystals by forming a bulk aggregate from their dispersions, scalable polycrystalline materials with more efficient mechanical and thermal energy transfers will be produced. However,

crystallites often have disordered structures or defects at their surfaces<sup>5,8</sup>, hindering efficient energy transfer.

Herein, we report that grain boundaries within an aggregate of a-few-nanometers-wide crystalline cellulose nanofibers (CNFs) were crystallized by enhancing the inter-CNF interactions. CNFs are stainable materials with excellent mechanical and thermal properties, which are produced as a water dispersion using wood pulps as the raw material<sup>9</sup>. Their elemental unit is a crystallite consisting of uniaxially oriented molecular chains, known as a cellulose microfibril<sup>10,11</sup>. In the dispersion, the surface molecules of CNFs have a thermodynamically stable, non-crystalline conformation and are uniaxially oriented, similar to the inner crystalline molecules<sup>11-13</sup>.

We previously showed that the crystallinity of CNFs significantly decreased when aggregated microfibrils in a pulp dispersed as CNFs or separated into individual crystallites<sup>12</sup>. This phenomenon was interpreted to result from the exposure of the grain boundary that was partially crystallized in the microfibril aggregates. This study was aimed at recovering the decreased crystallinity of the CNFs by assembly. We also verified if the crystallization of the grain boundary led to greater efficiency in the thermal energy transfer of bulk crystal aggregates.

### **Aggregating CNFs**

Scheme 1 shows the procedure for enhancing the inter-CNF interactions in a bulk aggregate. The CNF dispersion was prepared by wet disintegration of a TEMPO-oxidised wood pulp<sup>14</sup>. In the TEMPO-oxidation reaction, the C6 hydroxy groups exposed on the microfibril surfaces are regioselectively oxidised, such that the resulting CNFs possess a high surface density of carboxy groups (up to ~1.7 groups per square nanometer). The carboxy groups are Na<sup>+</sup> type at the initial step. By the dissociation of the carboxy groups, the CNFs are stably dispersed in water and spontaneously form a nematic liquid-crystalline phase where the CNFs are uniaxially oriented in places (Scheme 1a)<sup>15</sup>. In this study, the nematic-ordered CNF dispersion was assembled into dry sheets by two processes. One process was freeze drying from a 30% tert-butyl alcohol-containing diluted dispersion, followed by pressing of the dried aerogel-like

product (sample *i*)<sup>16</sup>. The other process was evaporative drying *via* solvent casting of the CNF dispersion at 40 °C under a high relative humidity of 80%, resulting in the formation of transparent and flat dry sheets (sample *ii*)<sup>17</sup>. Sample *ii* was further processed with a dilute acid solution to convert the carboxy groups from sodium salt into protonated acid form, H type (sample *iii*, see Figure S1a for the evidence of protonation)<sup>18</sup>, followed by a hydrothermal treatment using a common autoclave at 135 °C and 212 kPa (sample *iv*). The hydrothermal treatment was adopted to enable the CNFs to rearrange and stabilise their interaction. The CNFs remained solid, without melting or dissolving, under the conditions adopted in this study.

The assembled state of the CNFs in each sheet is illustrated in Scheme 1b: roughly oriented in sample *i*, and highly oriented in samples *ii–iv*. Meanwhile, the CNFs of samples *i–iv* were on average packed parallel to the sheet surface (see Figures S2 for X-ray diffraction (XRD) diagrams)<sup>17</sup>. The CNFs in samples *iii* and *iv* were also hydrogen-bonded with one another *via* the surface carboxy groups, as analysed by Fourier-transform infrared (FTIR) spectroscopy (Figure S1a), and those in sample *iv* were more strongly hydrogen-bonded (Figure S1b,c). Accordingly, the porosity of the samples decreased in the order of sample *i* > *ii* > *iii* > *iv*, at 16%, 10%, 9%, and 4%, respectively. The specific surface area (SSA) of sample *i* was ~6.3 m<sup>2</sup> g<sup>-1</sup>, as measured by nitrogen adsorption analysis (Figure S3), whereas those of samples *ii*, *iii*, and *iv* were all below the limit of detection (~2 m<sup>2</sup> g<sup>-1</sup>). Therefore, the CNFs in each sample were considered to interact more closely or strongly in the order of sample *i* < *ii* < *iii* < *iv*.

### Recovery of Crystallinity

Figure 1a shows powder XRD profiles of the oxidised starting pulp and CNF samples *i–iv*. The XRD profiles of the pulp and sample *i* notably differed; all the peaks broadened and their intensities decreased. From sample *i* to *ii*, the peak widths narrowed. From sample *iii* to *iv*, the peaks further sharpened and intensified, and the (2 0 0) peak shifted slightly to the high-angle side. Finally, sample *iv* exhibited a distinct XRD profile rather than the starting pulp.

The nuclear magnetic resonance (NMR) spectra for the samples are shown in Figure 1b. In the C4 and C6 regions of the NMR spectra, the crystalline signals centred at 88 ppm (C4) and 65 ppm (C6) remarkably decreased at the first step of the pulp–

sample *i* conversion and increased in the order of samples *ii*, *iii*, and *iv*. Meanwhile, the non-crystalline signals at 84 ppm (C4) and 62 ppm (C6) increased at the first step and then decreased in the order of samples *ii*, *iii*, and *iv*.

As measures of the crystallinity, the Scherrer's crystal sizes of the (2 0 0) plane and crystallinity indices were calculated from the XRD profiles and NMR spectra, respectively (Figure 1c,d)<sup>12</sup>. The crystallinity indices were expressed in two different ways as the area ratios of the crystalline and non-crystalline signals in the C4 and C6 regions. Note that the crystalline C6 signal arises from the C6 carbon atoms turning the C6–O6 bond to the “*trans-gauche (tg)*” configuration against the C5–O5/C4–C5 bonds in anhydroglucose units<sup>11</sup>, and that the crystalline C4 conformation is fixed with the intra/inter-molecular hydrogen bonds *via* the *tg*-configurational C6 hydroxy groups. The crystallinity indices reflected the degree of intra-/inter-molecular hydrogen bonds.

The (2 0 0) crystal size decreased from 3.5 nm to 2.0 nm by the pulp–sample *i* conversion, and increased up to 3.8 nm in the order of samples *ii*, *iii*, and *iv* (Figure 1c). This increase in the crystal size explained the slight shift of the (2 0 0) peak position to the high-angle side, according to a previous report<sup>19</sup>. Also, the two crystallinity indices of the C4 and C6 carbon atoms decreased by ~30% from 40–50% on the conversion to sample *i*, and then increased by ~30% for samples *ii*, *iii*, and *iv* (Figure 1d). For both the crystal size and crystallinity index, the initial decrease was interpreted to result from the increase in SSA by disintegration of the pulp into the CNF dispersion (see Introduction)<sup>12</sup>. The successive increase was thus attributed to assembly of the CNFs in dry sheets; the inter-CNF interaction was dominant in the recovery of crystallinity.

Interestingly, the final values for sample *iv* reached or even surpassed the crystal size and crystallinity indices of the starting pulp; the crystallinity of the CNFs was reversible (see Figure S4 for the repeatability data). The recovery of crystallinity was also demonstrated for other type of CNFs produced from chemically unmodified, raw pulps solely by wet disintegration (Figure S5). Furthermore, other fibrillar crystallites of  $\alpha$ -chitin showed the recovery of crystallinity through the same process as the dispersion and assembly of CNFs in this study (Figure S6).

### **Inter-CNF interactions**

The contribution of the inter-CNF interactions to the recovery of crystallinity was investigated in more detail using two additional surface-modified CNFs (Figure 2a): hydrophobic CNFs bearing bulky tetra-*n*-butylammonium (TBA) as the counterion of the surface carboxy group<sup>20</sup>; and polymer-covered CNFs adsorbing an amorphous, hydroxyethyl cellulose by ~10% w/w<sup>21</sup>. The adsorption of 10% roughly corresponded to two HEC molecules per single CNF. These two CNF dispersions were assembled into transparent dry sheets through the same drying process as adopted in the preparation of samples *ii* and *iii*.

The TBA-bearing CNFs exhibited a significant recovery of the (2 0 0) crystal size (Figure 2b), whereas their crystallinity index stayed as low as 14% (Figure 2c). These results provided a deeper understanding of the recovery of crystallinity. The TBA ions were coupled with carboxy groups localised on the hydrophilic (1 1 0) and (1 -1 0) surfaces (see inset in Figure 1a), such that the hydrophobic (2 0 0) surface was exposed. Thus, the recovery of the crystal size indicated that TBA-bearing CNFs were stacked on the exposed (2 0 0) plane. Meanwhile, the low crystallinity index indicated that the inter-CNF hydrogen bonds between the hydrophilic surfaces were inhibited by the bulky TBA ions.

The HEC-covered CNFs showed different behaviours, in that both the crystal size and crystallinity index slightly increased (Figure 2b,c). HEC is amphiphilic, such that the whole surface of the CNFs were sparsely covered with HEC at a CNF/HEC ratio of 9:1. The results in Figure 2b,c for the HEC-covered CNFs were thus attributed to “partially-blocked” inter-CNF interactions.

These results supported that the inter-CNF interactions were dominant in the recovery of crystallinity, indicating that the inter-CNF (2 0 0) stacking and hydrogen bonding contributed mainly to the recovery of the crystal size and crystallinity index, respectively, which was also supported by the results for samples *ii* and *iii* in Figure 1c,d. From the Na<sup>+</sup>-type sample *ii* to the hydrogen-bonded H-type sample *iii*, the (2 0 0) crystal size was approximately constant, whereas the crystallinity index significantly increased.

It is well known as a phenomenon “hornification” in the field of wood pulp and paper sciences that the crystallinity of cellulosic samples including CNFs slightly increases by the repeating cycle of wet–dry states<sup>22,23</sup>. This phenomenon has been

ambiguously interpreted to result from enhancement of the degree of hydrogen bonding in samples by drying, and its mechanism remains unclear. The results in this study suggested that hornification is based on inter-microfibril (2 0 0) stacking and hydrogen bonding.

### **Simulation**

To assess the major configuration of CNFs in the interactions, an XRD profile of sample *iv* was compared with simulated profiles of possible inter-CNF configurations (Figures 3 and S7). The experimental profile was obtained by azimuthally integrating an XRD diagram of a sample *iv* sheet set parallel to the beam. We assumed no specific orientation of the crystal planes to the sheet surface by considering: 1) the similarity of the experimental profile in Figure 3 with that obtained by the reflection method for sample *iv* in Figure 1a, and 2) the twisting structure of the CNFs around the crystallographic *c* axis<sup>24-26</sup>.

In the simulation, the structure of the single CNFs was assumed to be composed of 18 cellulose chains with a stacking mode of 2/3/4/4/3/2, based on previous reports on the morphological analyses of single CNFs<sup>12,27</sup>. This 18-chain model had flat two-molecule-wide (2 0 0) surfaces, enabling the CNFs to stably stack on the (2 0 0) plane (see the results for TBA-bearing CNFs in Figure 2). As shown in Figure 3, the CNFs assembled parallel to one another along the *c* axis. Simulations of antiparallel assembly are shown in Figure S7. Coupling of only two CNFs was simulated here for simplicity but the reality should be more complex.

The highest  $R^2$  value (0.897) was obtained for configuration #12, where the modelled CNFs coupled facing their (1 1 0) surfaces<sup>28</sup>. This configuration allowed the CNFs to form inter-CNF hydrogen bonds, explaining the recovery of the crystal size and crystallinity index for sample *iv*. In addition, the (1 1 0) plane had a larger surface free energy than the other planes<sup>29</sup>. The CNF coupling for configuration #12 thus reduced the free energy in the system to a greater extent and was the most stable of the possible inter-CNF configurations. The XRD profile of the starting pulp (Figure 1a) also showed the best fit ( $R^2 = 0.883$ ) with configuration #12. A similar result held for the antiparallel assembly shown in Figure S5; the best fit ( $R^2 = 0.875$ ) was achieved at a configuration that significantly reduced the (1 1 0) surface. In the antiparallel assembly,

there existed no configuration where the CNFs coupled by facing the same crystal plane.

Configuration #7 matched the experimental profile in terms of peak shape, especially at lower angles of  $\sim 15^\circ$ . However, its coefficient of correlation,  $R^2$  (0.826), was the lowest (see Methods for the  $R^2$  calculation). This gap was because the intensity ratio of the (2 0 0) plane and combined (1 -1 0)/(1 1 0) peaks in the simulation was significantly different from the corresponding ratio for the experimental profile; on closer inspection, the position of the combined (1 -1 0)/(1 1 0) peak in the simulation was shifted by  $\sim 1^\circ$  from the experimental peak.

## Modelling

The recovery of the (2 0 0) crystal size was easily interpreted as the phase extension of the (2 0 0) plane by CNF assembly. However, the mechanism for the recovery of crystallinity index must be considered. In Figure 1d, the C4- and C6-derived crystallinity indices were coordinated and recovered from the lowest degree of 15% (sample *i*) by up to  $\sim 30\%$  (sample *iv*). Considering that most of the C6 hydroxy groups exposed on the CNF surface were converted to carboxy groups, the recovery of crystallinity index was interpreted to result from conformational changes not only of the residual surface C6 hydroxy group but also of the interior of each CNF structure *via* inter-CNF hydrogen bonding.

Figure 4 illustrates a model for the conformational changes induced by the inter-CNF hydrogen bonding. Three cases were assumed based on the hydrogen-bonding mode in the cellulose I type structure<sup>11</sup>. In case 1, the residual surface C6 hydroxy groups take the *tg* conformation from other noncrystalline states (*gt* or *gg*, see the section “Recovery of Crystallinity”). This change was the most plausible, but the maximum contribution to the recovery of crystallinity index was estimated to be  $\sim 10\%$ , which was insufficient for explaining the recovery of 30%. Cases 2 and 3 describe the conformational changes occurring at the interior of each CNF structure. In case 2, the C6 hydroxy groups in the surface molecules of each CNF facing inside adopt the *tg* conformation. In case 3, the C6 hydroxy groups in the interior molecules facing the surface molecules adopt the *tg* conformation. These two cases were assumed to result

from some restraint imposed on the surface molecules *via* the inter-CNF hydrogen bonding.

### **Bulk properties**

The recovery of crystallinity was expected to improve the bulk properties of the CNF structures. Figure 5 shows the thermal diffusivity,  $\alpha$ , and conductivity,  $k$ , of samples *i–iv* as a function of the crystallinity index. With the recovery of crystallinity, both the diffusivity and conductivity significantly improved (see Figure S8 for the specific values of  $\alpha$  and  $k$  divided by their bulk densities, showing the same trend). This trend is reasonable because heat transfers in a solid via phonon propagation. The phonon is an elastic wave and is often scattered at the grain boundary in a particle assembly. The recovery of crystallinity was caused by the inter-CNF interactions, which reduced the grain boundary and facilitated phonon propagation.

### **Conclusions and perspectives**

Enhancing the interaction between CNFs or a-few-nanometer-wide fibrillar crystallites of cellulose resulted in the coupling of multiple crystallites into single fusion crystals in a bulk aggregate without passing through a melting or dissolving state. The interaction was enhanced by the following steps: starting from a nematic liquid-crystalline dispersion where the CNFs were uniaxially oriented in places, forming a dense aggregate by condensation, and enabling the CNFs to bind with one another *via* hydrogen bonds at the grain boundary. These steps induced the conformational change of the constituent carbon atoms of the CNFs to be crystalline, and the phase extension of the crystal planes occurred. Accordingly, the lowered crystallinity of the CNFs, which was previously considered irreversible, was recovered, and thermal energy transfer in the aggregate was significantly improved. CNFs have recently been produced in industrial settings, *e.g.* capacity ~1000 tons in Japan in 2020<sup>30</sup>, and this finding will contribute to the building of the technical bases for exploiting the potential of CNFs in bulk materials. This finding offers a deeper understanding of “hornification”, which has been ambiguously interpreted in the field of wood pulp and paper sciences. Furthermore, other fibrillar crystallites of  $\alpha$ -chitin showed a similar fusion phenomenon

through the enhancement of their inter-crystallite interactions. Crystallite fusion in aggregates may occur for other biopolymers.

### Online content

Any methods, additional references, supplementary information, acknowledgements, details of author contributions, and competing interests are available at

<https://doi.org/XXX>

### References

1. Ashby, M. F., Shercliff, H. & Cebon, D. *Materials: Engineering, Science, Processing and Design* (Elsevier, 2013)
2. French, A. D., Pérez, S., Bulone, V., Rosenau, T. & Gray, D. *Encyclopedia of Polymer Science and Technology* 1-69 (Wiley, 2018)
3. Shan, Z. *et al.* Grain boundary-mediated plasticity in nanocrystalline nickel. *Science* **305**(5684), 654-657 (2004). [10.1126/science.1098741](https://doi.org/10.1126/science.1098741), Pubmed:[15286368](https://pubmed.ncbi.nlm.nih.gov/15286368/)
4. Qian, X., Zhou, J. & Chen, G. Phonon-engineered extreme thermal conductivity materials. *Nat. Mater.* (2021). [10.1038/s41563-021-00918-3](https://doi.org/10.1038/s41563-021-00918-3), Pubmed:[33686278](https://pubmed.ncbi.nlm.nih.gov/33686278/)
5. Huang, P. Y. *et al.* Grains and grain boundaries in single-layer graphene atomic patchwork quilts. *Nature* **469**(7330), 389-392 (2011). [10.1038/nature09718](https://doi.org/10.1038/nature09718), Pubmed:[21209615](https://pubmed.ncbi.nlm.nih.gov/21209615/)
6. Podsiadlo, P. *et al.* Ultrastrong and stiff layered polymer nanocomposites. *Science* **318**(5847), 80-83 (2007). [10.1126/science.1143176](https://doi.org/10.1126/science.1143176), Pubmed:[17916728](https://pubmed.ncbi.nlm.nih.gov/17916728/)
7. Hou, Y. *et al.* Strengthening and toughening hierarchical nanocellulose via humidity-mediated interface. *ACS Nano* **15**(1), 1310-1320 (2021). [10.1021/acsnano.0c08574](https://doi.org/10.1021/acsnano.0c08574), Pubmed:[33372752](https://pubmed.ncbi.nlm.nih.gov/33372752/)
8. Goris, B. *et al.* Atomic-scale determination of surface facets in gold nanorods. *Nat. Mater.* **11**(11), 930-935 (2012). [10.1038/nmat3462](https://doi.org/10.1038/nmat3462), Pubmed:[23085569](https://pubmed.ncbi.nlm.nih.gov/23085569/)
9. Li, T. *et al.* Developing fibrillated cellulose as a sustainable technological material. *Nature* **590**, 47-56 (2021). [10.1038/s41586-020-03167-7](https://doi.org/10.1038/s41586-020-03167-7), Pubmed: [33536649](https://pubmed.ncbi.nlm.nih.gov/33536649/)
10. Cosgrove, D. J. Growth of the plant cell wall. *Nat. Rev. Mol. Cell Biol.* **6**(11), 850-861 (2005). [10.1038/nrm1746](https://doi.org/10.1038/nrm1746), Pubmed:[16261190](https://pubmed.ncbi.nlm.nih.gov/16261190/)
11. Nishiyama, Y., Langan, P. & Chanzy, H. Crystal structure and hydrogen-bonding system in cellulose I $\beta$  from synchrotron X-ray and neutron fiber diffraction. *J. Am. Chem. Soc.* **124**(31), 9074-9082 (2002). [10.1021/ja0257319](https://doi.org/10.1021/ja0257319), Pubmed:[12149011](https://pubmed.ncbi.nlm.nih.gov/12149011/)
12. Daicho, K., Saito, T., Fujisawa, S. & Isogai, A. The crystallinity of nanocellulose: Dispersion-induced disordering of the grain boundary in biologically structured cellulose. *ACS Appl. Nano Mater.* **1**(10), 5774-5785 (2018). [10.1021/acsanm.8b01438](https://doi.org/10.1021/acsanm.8b01438)
13. Fernandes, A. N. *et al.* Nanostructure of cellulose microfibrils in spruce wood. *Proc. Natl Acad. Sci. U. S. A.* **108**(47), E1195-E1203 (2011). [10.1073/pnas.1108942108](https://doi.org/10.1073/pnas.1108942108), Pubmed:[22065760](https://pubmed.ncbi.nlm.nih.gov/22065760/)
14. Saito, T., Nishiyama, Y., Putaux, J. L., Vignon, M. & Isogai, A. Homogeneous suspensions of individualized microfibrils from TEMPO-catalyzed oxidation of native cellulose. *Biomacromolecules* **7**(6), 1687-1691 (2006). [10.1021/bm060154s](https://doi.org/10.1021/bm060154s), Pubmed:[16768384](https://pubmed.ncbi.nlm.nih.gov/16768384/)

15. Saito, T., Uematsu, T., Kimura, S., Enomae, T. & Isogai, A. Self-aligned integration of native cellulose nanofibrils towards producing diverse bulk materials. *Soft Matter* **7**(19), 8804-8809 (2011). [10.1039/c1sm06050c](https://doi.org/10.1039/c1sm06050c)
16. Nemoto, J., Saito, T. & Isogai, A. Simple freeze-drying procedure for producing nanocellulose aerogel-containing, high-performance air filters. *ACS Appl. Mater. Interfaces* **7**(35), 19809-19815 (2015). [10.1021/acsami.5b05841](https://doi.org/10.1021/acsami.5b05841), Pubmed:[26301859](https://pubmed.ncbi.nlm.nih.gov/26301859/)
17. Zhao, M. *et al.* Nematic structuring of transparent and multifunctional nanocellulose papers. *Nanoscale Horiz.* **3**(1), 28-34 (2018). [10.1039/c7nh00104e](https://doi.org/10.1039/c7nh00104e), Pubmed:[32254107](https://pubmed.ncbi.nlm.nih.gov/32254107/)
18. Shimizu, M., Saito, T. & Isogai, A. Water-resistant and high oxygen-barrier nanocellulose films with interfibrillar cross-linkages formed through multivalent metal ions. *J. Membr. Sci.* **500**, 1-7 (2016). [10.1016/j.memsci.2015.11.002](https://doi.org/10.1016/j.memsci.2015.11.002)
19. Huang, S. *et al.* Dehydration-induced physical strains of cellulose microfibrils in plant cell walls. *Carbohydr. Polym.* **197**, 337-348 (2018). [10.1016/j.carbpol.2018.05.091](https://doi.org/10.1016/j.carbpol.2018.05.091), Pubmed:[30007621](https://pubmed.ncbi.nlm.nih.gov/30007621/)
20. Shimizu, M., Saito, T. & Isogai, A. Bulky quaternary alkylammonium counterions enhance the nanodispersibility of 2,2,6,6-tetramethylpiperidine-1-oxyl-oxidized cellulose in diverse solvents. *Biomacromolecules* **15**(5), 1904-1909 (2014). [10.1021/bm500384d](https://doi.org/10.1021/bm500384d), Pubmed:[24750066](https://pubmed.ncbi.nlm.nih.gov/24750066/)
21. Zhou, Q. *et al.* Nanostructured biocomposites based on bacterial cellulosic nanofibers compartmentalized by a soft hydroxyethylcellulose matrix coating. *Soft Matter* **5**(21), 4124-4130 (2009). [10.1039/b907838j](https://doi.org/10.1039/b907838j)
22. Salmén, L. & Stevanic, J. S. Effect of drying conditions on cellulose microfibril aggregation and “hornification”. *Cellulose* **25**(11), 6333-6344 (2018). [10.1007/s10570-018-2039-1](https://doi.org/10.1007/s10570-018-2039-1)
23. Peng, Y. *et al.* Influence of drying method on the material properties of nanocellulose I: thermostability and crystallinity. *Cellulose* **20**(5), 2379-2392 (2013). [10.1007/s10570-013-0019-z](https://doi.org/10.1007/s10570-013-0019-z)
24. Willhammar, T. *et al.* Local crystallinity in twisted cellulose nanofibers. *ACS Nano* **15**(2), 2730-2737 (2021). [10.1021/acs.nano.0c08295](https://doi.org/10.1021/acs.nano.0c08295), Pubmed:[33464042](https://pubmed.ncbi.nlm.nih.gov/33464042/)
25. Ogawa, Y. Electron microdiffraction reveals the nanoscale twist geometry of cellulose nanocrystals. *Nanoscale* **11**(45), 21767-21774 (2019). [10.1039/c9nr06044h](https://doi.org/10.1039/c9nr06044h), Pubmed:[31573012](https://pubmed.ncbi.nlm.nih.gov/31573012/)
26. Nyström, G., Arcari, M., Adamcik, J., Usov, I. & Mezzenga, R. Nanocellulose fragmentation mechanisms and inversion of chirality from the single particle to the cholesteric phase. *ACS Nano* **12**(6), 5141-5148 (2018). [10.1021/acs.nano.8b00512](https://doi.org/10.1021/acs.nano.8b00512), Pubmed:[29758157](https://pubmed.ncbi.nlm.nih.gov/29758157/)
27. Song, B., Zhao, S., Shen, W., Collings, C. & Ding, S. Y. Direct measurement of plant cellulose microfibril and bundles in native cell walls. *Front. Plant Sci.* **11**, 479 (2020). [10.3389/fpls.2020.00479](https://doi.org/10.3389/fpls.2020.00479), Pubmed:[32391038](https://pubmed.ncbi.nlm.nih.gov/32391038/)
28. Rosén, T. *et al.* Cross-Sections of Nanocellulose from Wood Analyzed by Quantized Polydispersity of Elementary Microfibrils. *ACS Nano* **14**(12), 16743-16754 (2020). [10.1021/acs.nano.0c04570](https://doi.org/10.1021/acs.nano.0c04570), Pubmed:[33253525](https://pubmed.ncbi.nlm.nih.gov/33253525/)
29. Oehme, D. P. *et al.* Gaining insight into cell wall cellulose macrofibril organisation by simulating microfibril adsorption. *Cellulose* **22**(6), 3501-3520 (2015). [10.1007/s10570-015-0778-9](https://doi.org/10.1007/s10570-015-0778-9)
30. See, for example, the website of Nanocellulose Japan, Available from: <https://www.nanocellulosejapan.com/>

## Online content

### Methods

**Materials.** A softwood dissolving pulp (Nippon Paper Industries, Japan) was used as the starting sample. TEMPO, or 2,2,6,6-tetramethylpiperidine-1-oxyl, was purchased from Sigma-Aldrich, Japan. All other chemicals were purchased from FUJIFILM Wako Pure Chemical Corporation, Japan and were used without any modification.

**CNF dispersion.** The pulp (1 g) was TEMPO-oxidised with the addition of NaClO (5 mmol per gram of sample) according to a previous report<sup>14</sup>. The oxidised samples were then treated with NaBH<sub>4</sub> (0.1 g) in water (100 mL) at pH 10 for 3 h to eliminate unstable aldehyde groups. The carboxylate content of the oxidised pulp was determined to be ~1.3 mmol/g by conductivity titration. The oxidised pulp was suspended in water (0.1% w/w) and mechanically treated by using a Microtec Physcotron NS-56 homogenizer equipped with a 20-mm diameter shaft at 7500 rpm for 5 min, followed by sonication using a Nihon Seiki US-300T ultrasonic homogenizer equipped with a 26-mm diameter tip at 70% output for 4 min. A part of the unfibrillated fraction in the dispersion was removed by centrifugation at 12000 g for 10 min, and the supernatant was collected as the CNF dispersion.

**CNF sheets.** The CNF dispersion was subjected to freeze drying or evaporative drying. The dispersion (0.1%) was freeze-dried from a 30% *tert*-butyl alcohol-containing wet state according to a previously reported method<sup>16</sup>. The freeze-dried CNF was conditioned at 23 °C and 50% relative humidity, followed by pressing at ~750 MPa for 1 min to obtain an aerogel-like sheet (sample *i*). The dispersion was concentrated to 0.4% at 40 °C using an evaporator, and then poured into a 90-mm diameter polystyrene petri dish, followed by evaporative drying at 40 °C and 80% relative humidity for over a week (sample *ii*)<sup>17</sup>. The resulting CNF sheet was immersed in a 0.1 M HCl aqueous solution for 2 h, followed by washing with distilled water and drying at 40 °C and 80% relative humidity (sample *iii*). Sample *iii* was placed in a glass petri dish and further subjected to hydrothermal treatment using a LSX-500 autoclave at 135 °C and 212 kPa

for 30 min. The resulting film was gently washed with distilled water, followed by drying at 40 °C and 80% relative humidity (sample *iv*). All samples were conditioned at 23 °C and 50% relative humidity before analysis.

**TBA-bearing CNF.** The oxidised pulp suspension (0.1%) was mixed with 0.1 M HCl for 2 h. After washing with distilled water, the pulp was neutralised with 10% *tetra-n*-butylammonium (TBA) hydroxide according to a previously reported method<sup>31</sup>. The TBA-bearing CNF dispersion was then dried at 40 °C and 80% relative humidity, and conditioned at 23 °C and 50% relative humidity before the analyses.

**HEC-covered CNF.** The Na<sup>+</sup> type of the 0.1% CNF dispersion was mixed with a 10% w/w hydroxyethyl cellulose solution (degree of substitution, 1.6–1.8)<sup>21</sup>, and subsequently dried and conditioned in the same manner as the TBA-bearing CNF.

**XRD.** XRD measurements were performed in the reflection and transmission modes. In the reflection mode, the XRD profiles were obtained at diffraction angles  $2\theta$  ranging from 3–45° using a Rigaku Mini Flex diffractometer with Ni-filtered Cu K $\alpha$  radiation ( $\lambda = 0.1542$  nm) at 40 kV and 15 mA. The crystal size was calculated from the XRD peak corresponding to the (2 0 0) plane using Scherrer's equation (with a shape factor  $K = 0.9$ ). Peak separation was performed according to a previous report<sup>12</sup>. In the transmission mode, the XRD diagrams was recorded on a Fujifilm imaging plate (2540  $\times$  2540 pixels, 50  $\times$  50  $\mu\text{m}^2$ ) at room temperature using a Rigaku MicroMax-007 HF system operating at 40 kV and 30 mA with Cu K $\alpha$  radiation ( $\lambda = 0.15418$  nm). The samples were set parallel to the X-ray beam, and the distance between the sample and imaging plate was calibrated using NaF. The recorded diagram was read using a Rigaku RAXIA-Di system and converted to a one-dimensional  $2\theta$ -intensity and azimuthal profiles using a Rigaku 2DP software. The degree of orientation (DO) was calculated from the azimuthal profile of the (2 0 0) reflection using the following equation<sup>17</sup>:

$$DO = \frac{180^\circ - FWHM}{180^\circ},$$

where FWHM is the full width at half maximum.

**CP/MAS  $^{13}\text{C}$  NMR spectroscopy.** CP/MAS  $^{13}\text{C}$  NMR measurements were performed using a JEOL JNM-ECAII 500 spectrometer (JEOL Ltd., Tokyo, Japan) equipped with a 3.2-mm HXMAS probe and ZrO<sub>2</sub> rotors at 125.77 MHz for  $^{13}\text{C}$ . The samples were spun at 15000 Hz and the 90° proton decoupler pulse width, contact time, and relaxation delay were set to 2.5  $\mu\text{s}$ , 2 ms, and 5 s, respectively<sup>32</sup>. Adamantane was used as the internal standard for the  $^{13}\text{C}$  chemical shifts. The C4 and C6 crystallinity indices were calculated as the area ratio of the crystalline and noncrystalline signals in the C4 and C6 regions, respectively. Peak separation was performed according to the method described in a previous report<sup>12</sup>.

**XRD simulation.** The single CNF model consisting of 18 cellulose chains was constructed using a Visualizer module in the BIOVIA Material Studio 2020 software, based on the atomic coordinates of the crystal unit of cellulose I $\beta$  crystallite, reported by Nishiyama *et al.*<sup>11</sup>. In the 18-chain model, the cellulose molecular sheets were stacked in 2/3/4/4/3/2 chain modes with crystal sizes of the (110), (1-10), and (200) planes of 3.10 nm, 2.12 nm, and 2.34 nm, respectively<sup>12</sup>. The model was extended by two cellobiose units along the *c* axis, according to previous reports<sup>33</sup>. The 23 types of model where two single CNFs were assembled were constructed as shown in Figures 3 and S7. The XRD patterns of these models were simulated using a Forcite module in the software based on Debye's scattering formula:

$$I(Q) = \sum_i \sum_j f_i f_j \frac{\sin(Qr_{ij})}{Qr_{ij}},$$

where  $Q$  is the scattering vector, described as  $Q = |Q| = \frac{4\pi \sin\theta}{\lambda}$  ( $\theta$ : the diffraction half-angle,  $\lambda$ : wavelength),  $f_i$  and  $f_j$  are the atomic scattering factors of the radiation used, and  $r_{ij}$  denotes the vector connecting atoms  $i$  and  $j$ . The X-ray and cut-off wavelengths for the calculation were set to 1.54178 and 40  $\text{\AA}$ , respectively. For comparing the simulated XRD patterns with the experimental pattern, the correlation coefficient,  $R^2$ , was calculated using the following equation:

$$R^2 = \frac{\sum(x-x')(y-y')}{\sqrt{\sum(x-x')^2 \sum(y-y')^2}},$$

where  $x$  and  $y$  are the relative intensities of the simulated and experimental XRD in the range of  $2\theta = 12\text{--}32^\circ$ , respectively; and  $x'$  and  $y'$  are average intensities of the simulated and experimental XRD, respectively.

**Thermal properties.** The thermal diffusivity,  $\alpha$ , values in the out-of-plane direction of samples *i-iv* were measured at over 10 different locations using thermal wave analysis with an ai-Phase Mobile 1u at 23 °C and 50% relative humidity. The applied voltage was 0.8 V, and the delay in the phase of the temperature wave (with an amplitude of  $\pm 0.5$  °C) was measured at 10 points within a range of 6–60 Hz for each sheet pot. The integration time for each point was typically 10 s. During the measurement, the entire device was covered with an optically opaque windshield. The thermal conductivity,  $k$ , was calculated from  $\alpha$  using the following equation:

$$k = \alpha c \rho,$$

where  $c$  is the specific heat capacity, and  $\rho$  is the bulk density. The specific heat capacity  $c$  was measured using a Perkin Elmer DSC8500 instrument in the temperature range of 0–40 °C at a heating rate of 10 °C/min.

**Other analyses.** The porosities of the samples were calculated using the following equation:

$$\text{porosity} = \frac{1 - \text{Bulk density} \times (1 - \text{Moisture content})}{\text{true density}}.$$

The true densities were measured using a BELPycno helium pycnometer according to a previously reported method<sup>34</sup>. The bulk densities were calculated from their volumes and weights at 23 °C and 50% relative humidity. The moisture contents were calculated from the sample weights at 23 °C and 50% relative humidity and those after drying at 105 °C for 3 h. The scanning electron microscopy (SEM) images were captured with a Hitachi S-4800 field-emission microscope at 1 kV. The samples were pretreated with a Meiwafoxis Neo osmium coater at 5 mA for 10 s. The nitrogen adsorption–desorption isotherm was measured with a Quantachrome NOVA 4200e at  $-196$  °C after degassing the samples in the system at 105 °C for 3 h. The SSA values of the samples were estimated from the isotherms according to Brunauer-Emmett-Teller theory. The sample weights were measured after degassing.

- 31 Shimizu, M., Saito, T. & Isogai, A. Water-Resistant and High Oxygen-Barrier Nanocellulose Films with Interfibrillar Cross-Linkages Formed through Multivalent Metal Ions. *J. Membr. Sci.* **500**, 1 (2016).
- 32 Daicho, K., Fujisawa, S., Kobayashi, K., Saito, T. & Ashida, J. Cross-polarization dynamics and conformational study of variously sized cellulose crystallites using solid-state <sup>13</sup>C NMR. *Journal of Wood Science* **66**, 62, doi:[10.1186/s10086-020-01909-9](https://doi.org/10.1186/s10086-020-01909-9) (2020).
- 33 Kubicki, J. D. *et al.* The shape of native plant cellulose microfibrils. *Scientific reports* **8**, 1-8 (2018).
- 34 Daicho, K., Kobayashi, K., Fujisawa, S. & Saito, T. Crystallinity-Independent yet Modification-Dependent True Density of Nanocellulose. *Biomacromolecules* **21**, 3, doi:[10.1021/acs.biomac.9b01584](https://doi.org/10.1021/acs.biomac.9b01584) (2020).

## Acknowledgments

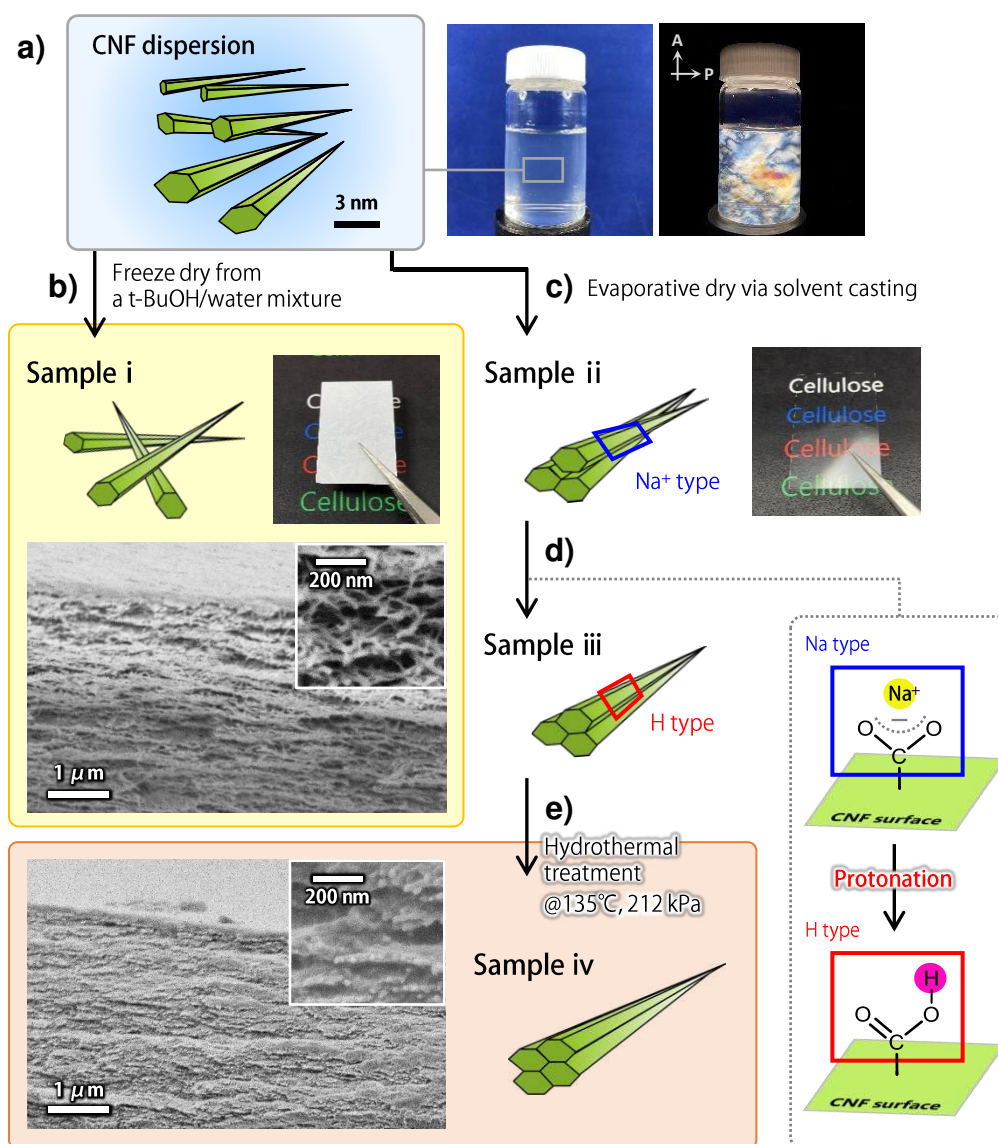
This research was partially supported by the JST-Mirai R&D Program (JPMJMI17ED), JSPS Grant-in-Aids for Scientific Research (18K14501; 20J12793; 20K15567; 21H04733), a PHOENIX Grant-in-Aid, and the Research Program for Next Generation Young Scientists of “Network Joint Research Center for Materials and Devices: Dynamic Alliance for Open Innovation Bridging Human, Environment and Materials” (20205012). We also thank Prof. Tomoya Imai at Kyoto University in Japan for fruitful discussion about the XRD analyses.

## Author Contributions

K.D. and T.S. conceived the concept of the study. K.D. and T.S. designed the experiments. K.D. performed all the experiments. All the authors analysed the data. K.D. and T.S. wrote the manuscript with contributions from all the authors.

## Completing Interests

The authors declare no competing interest.



**Scheme 1. Procedure for enhancing the inter-CNF interactions.** **a**, Schematic of the CNF dispersion forming a nematic liquid-crystalline phase, including its appearance and a birefringence image of the CNF dispersion. **b**, Conversion to sample *i*. Schematic of the assembled state of the CNFs in sample *i*, appearance, and cross-sectional SEM image. **c**, Conversion to sample *ii*. Schematic and appearance. **d**, Conversion to sample *iii*. Schematics of the assembled state and the protonation of the surface carboxy groups. **e**, Conversion to sample *iv*. Schematic and cross-sectional SEM image.

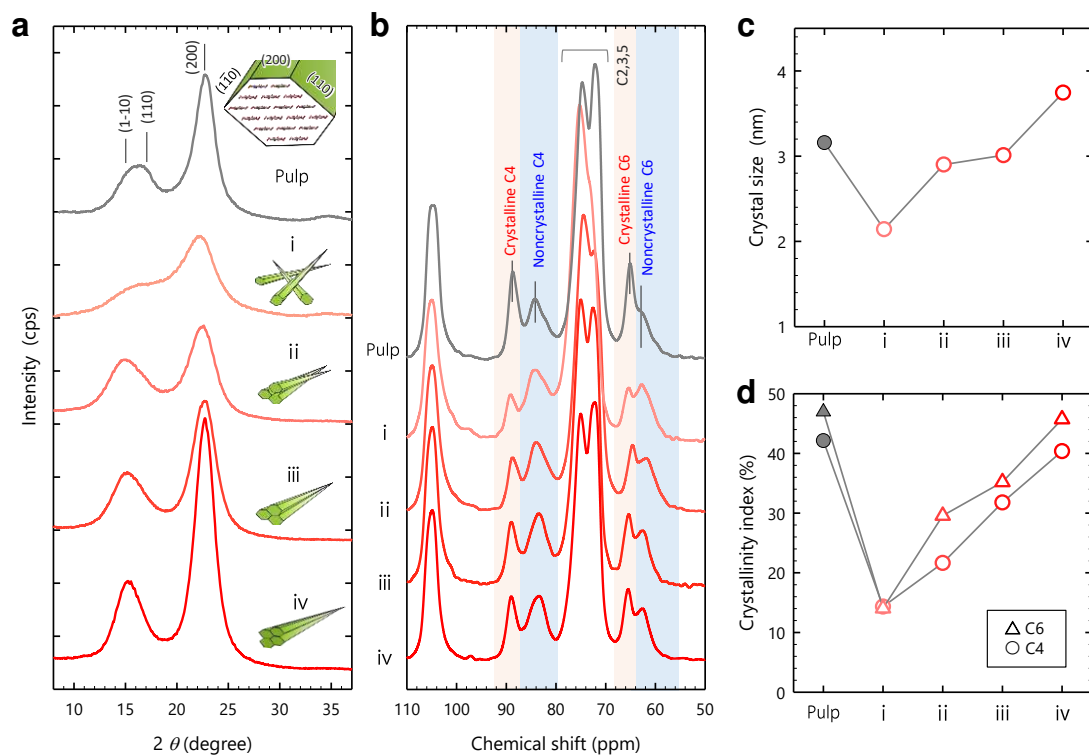


**Figure 1. Recovery of crystallinity.** **a**, XRD profiles, **b**, CP/MAS  $^{13}\text{C}$  NMR spectra of a series of samples ranging from the starting pulp to CNF samples *i–iv*. **c**, Crystal size of the (2 0 0) plane calculated from the XRD profiles, and **d**, crystallinity indices of the C4 and C6 carbon atoms calculated from the NMR spectra.

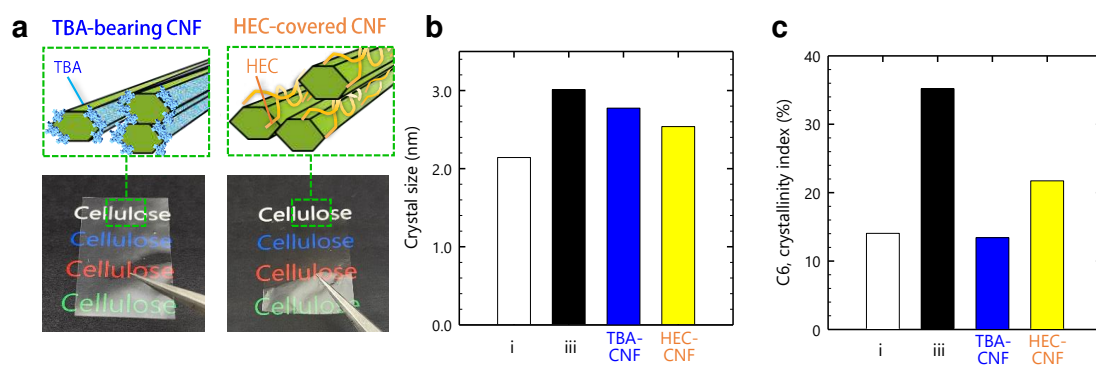


**Figure 2. Contribution of the inter-CNF interactions.** **a**, Schematics of the TBA-bearing and HEC-covered CNFs, and appearances of the samples. **b**, Crystal sizes, and **c**, crystallinity indices of the C6 carbon atoms of samples *i* and *iii*, and the TBA-bearing and HEC-covered CNFs.

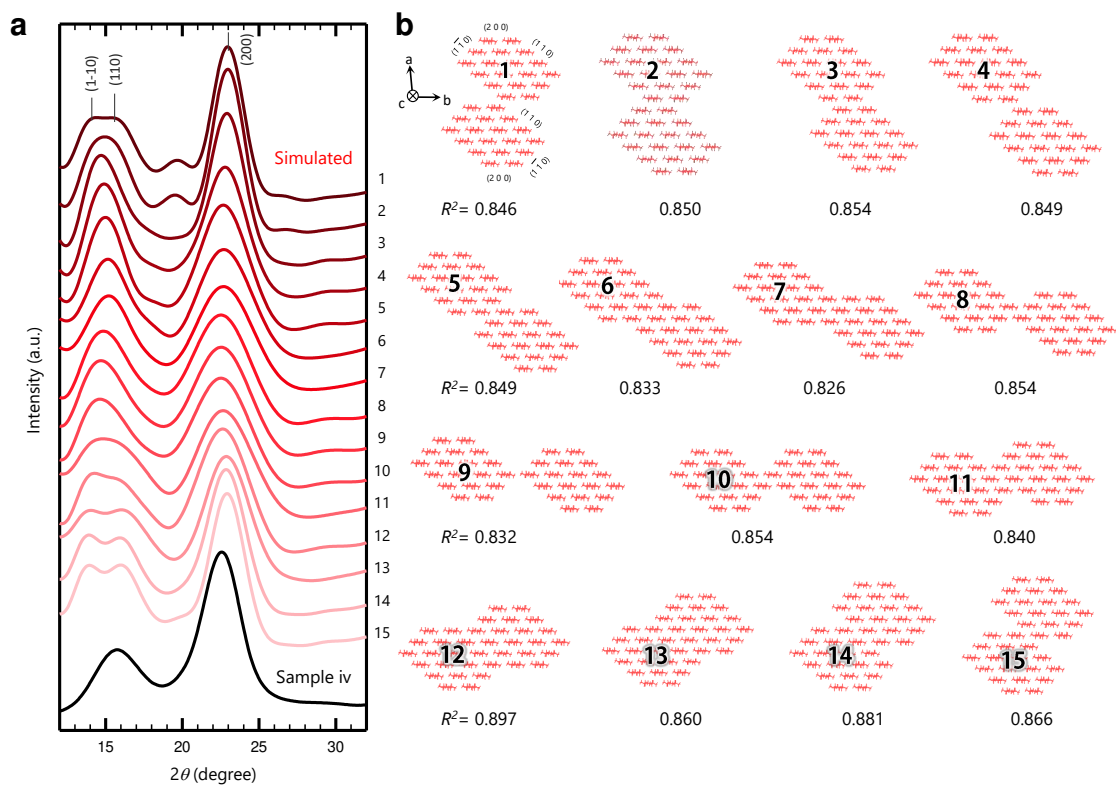


**Figure 3. Simulation. a, b,** Comparison of the XRD profile of sample *iv* with the simulated profiles of the possible inter-CNF configurations #1–15 **b**, The CNFs were assumed to assemble parallel to one another along the crystallographic *c* axis.

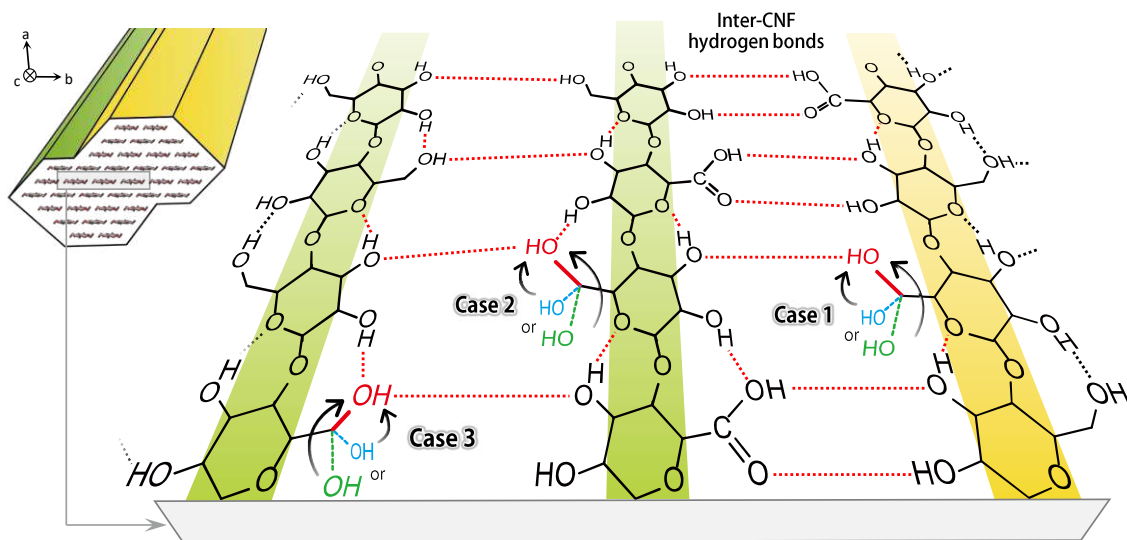


**Figure 4. Modelling.** A model for the conformational changes of the C6 carbon atoms induced by the inter-CNF hydrogen bonding.

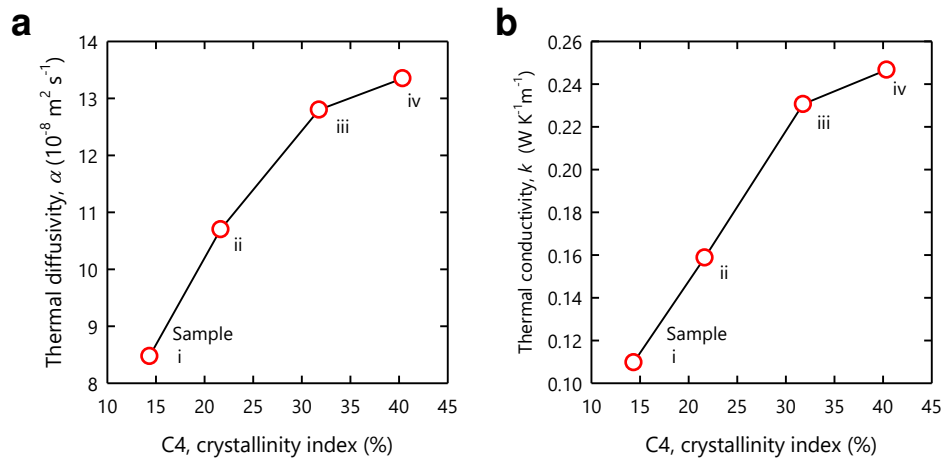


**Figure 5. Contribution to bulk properties. a**, Thermal diffusivity, and **b**, Conductivity of samples *i–iv* as a function of the crystallinity index of the C4 carbon atoms.

## Supplementary Files

This is a list of supplementary files associated with this preprint. Click to download.

- [SIDaicho.docx](#)